Mon. Not. R. Astron. Soc. **382,** 473–480 (2007) doi:10.1111/j.1365-2966.2007.12394.x

Limits on the 2.2-μm contrast ratio of the close-orbiting planet HD 189733b

J. R. Barnes,[1⋆] Travis S. Barman,[2] L. Prato,[2] D. Segransan,[3] H. R. A. Jones,[1] C. J. Leigh,[4] A. Collier Cameron[5] and D. J. Pinfield[1]

[1]*Centre for Astrophysics Research, University of Hertfordshire, Hertfordshire AL10 9AB*
[2]*Lowell Observatory, Planetary Research Centre, 1400 West Mars Hill Road, Flagstaff, AZ 86001, USA*
[3]*Observatoire de Genève, 51 Chemin des Maillettes, 1290 Sauverny CH, Switzerland*
[4]*Astrophysics Research Institute, Liverpool John Moores University, Birkenhead CH41 1LD*
[5]*SUPA, School of Physics and Astronomy, University of St Andrews, Fife KY16 9SS*

Accepted 2007 August 27. Received 2007 August 24; in original form 2007 July 20

ABSTRACT

We obtained 238 spectra of the close-orbiting extrasolar giant planet HD 189733b with resolution $R \sim 15\,000$ during one night of observations with the Near-Infrared High-Resolution Spectrograph (NIRSPEC), at the Keck II Telescope. We have searched for planetary absorption signatures in the 2.0–2.4 μm region where H_2O and CO are expected to be the dominant atmospheric opacities. We employ a phase-dependent orbital model and tomographic techniques to search for the planetary absorption signatures in the combined stellar and planetary spectra. Because potential absorption signatures are hidden in the noise of each single exposure, we use a model list of lines to apply a spectral deconvolution. The resulting mean profile possesses a signal-to-noise ratio (S/N) that is 20 times greater than that found in individual lines. Our spectral time series thus yields spectral signatures with a mean S/N = 2720. We are unable to detect a planetary signature at a contrast ratio of $\log_{10}(F_p/F_*) = -3.40$, with 63.8 per cent confidence. Our findings are not consistent with model predictions which nevertheless give a good fit to mid-infrared observations of HD 189733b. The 1σ result is a factor of 1.7 times less than the predicted 2.185-μm planet/star flux ratio of $\log_{10}(F_p/F_*) \sim -3.16$.

Key words: line: profiles – methods: data analysis – techniques: spectroscopic – stars: individual: HD 189733 – stars: late-type – planetary systems.

1 INTRODUCTION

A factor governing the atmospheric physics of the gas giants in our own Solar system is the relatively low temperatures of the surrounding environment. While internal heat sources and rotation play a role in atmospheric dynamics, much of the structure seen in the atmospheres is governed by chemical species which appear in relatively low abundance (∼1 per cent by mass) compared with a dominant makeup of Hydrogen and Helium. Extrasolar planetary atmospheres amenable to study must, however, differ considerably from the Solar system paradigm on account of their close proximity to their parent star.

Modern instrumentation is now capable of making observations of close-orbiting extrasolar giant planets (CEGPs) in order to learn about the physical make up of their atmospheres. Reflected light studies (Charbonneau et al. 1999; Collier Cameron et al. 1999, 2002; Leigh et al. 2003a,b) and more recent MOST photometry (Rowe et al. 2006) results have placed albedo *upper limits* on the atmospheres of CEGPs in the optical. While reflected light studies only search for an attenuated copy of the stellar light, they have the potential to yield important information about the chemical makeup of the planetary atmospheres. These upper limits to the planet/star contrast ratio have only been able to constrain CEGP atmospheres as having low reflectivity when compared with the Solar system gas giants.

The contrast between the planet and star in the infrared offers a more favourable regime in which to study CEGPs. An estimate of the temperature of a CEGP was first reported from 24-μm secondary eclipse measurements of HD 209458b by Deming et al. (2005). While a number of subsequent mid-infrared observations of other systems have now been made with the *Spitzer Space Telescope*, Harrington et al. (2006) were the first to report measurement of the phase-dependent flux of a CEGP, implying a world with a significant day-night temperature gradient. Such observations are now fuelling new research into the meteorology of extrasolar planets (Cooper & Showman 2005, 2006; Fortney et al. 2006). To obtain a fuller understanding of the atmospheres of CEGPs, it is important to study as wide a region of wavelength space as possible on CEGPs with a range of parameters.

⋆E-mail: j.r.barnes@herts.ac.uk

The detection of narrow absorption features due to molecular species is difficult in the optical because the atmospheres appear so dark whereas no high-resolution instrumentation in the thermal infrared is widely available. A number of contemporary instruments such as NIRSPEC at Keck (McLean et al. 1998), Infrared Camera and Spectrograph at Subaru (Kobayashi et al. 2000) and CRIRES at the Very Large Telescope (Kaüfl et al. 2004) are capable of making searches for absorption features in the near-infrared (near-IR) possible.

1.1 HD 189733

HD 189733b was the first planet to be discovered as a transiting planet spectroscopically (Bouchy et al. 2005). Observations taken around the time of transit indicated radial velocity anomalies due to the Rossiter–McLaughlin effect, where the transiting planet occults part of the stellar disc leading to a deviation from the measured Keplerian solution. Further spectroscopic observations were used to determine the spin-orbit alignment (Winn et al. 2006), indicating that the sky projections of the stellar spin axis and orbit normal are aligned to with $1\overset{\circ}{.}4 \pm 1\overset{\circ}{.}1$. Bakos et al. (2006b) used astrometric and radial velocity measurements to show that HD 189733 is the (K1V–K2V) primary (Bouchy et al. 2005) in a double star system with the secondary mid-M dwarf companion orbiting at 216 au from HD 189733 in a plane orthogonal to the orbit of HD 189733b.

The system parameters derived in the discovery paper by Bouchy et al. (2005) have since been refined through inclusion of multiband photometric transit observations by Bakos et al. (2006a). More recently, Winn et al. (2007) have also used photometric observations out of eclipse to determine a stellar rotation period of 13.4 d. A total of eight transits were used to determine the stellar and the planetary radii, and the photometric mid-transit ephemeris of H189733b which are $R_* = 0.753 \pm 0.025\,\mathrm{R}_\odot, R_\mathrm{p} = 1.156 \pm 0.046 R_\mathrm{J}$ and $T_\mathrm{c} = 2453\,988.803\,36(23) + 2.218\,5733(19)$ d, respectively (where the figures in brackets for the ephemeris denote the uncertainty in the last two decimal places). The values of $95\overset{\circ}{.}79 \pm 0\overset{\circ}{.}24$ (Bakos et al. 2006a) and $95\overset{\circ}{.}76 \pm 0\overset{\circ}{.}29$ determined for the inclination of the orbit of HD 189733b are in good agreement and remove the ambiguity in the planet's mass, yielding $M_\mathrm{p} = 1.13 \pm 0.03 M_\mathrm{J}$.

Because HD 189733b is one of the closest orbiting planets ($a = 0.0312 \pm 0.0004$ au) with a relatively late spectral type parent star, one would expect a relatively high planet/star contrast ratio, F_p/F_*. Deming et al. (2006) detected the strong infrared thermal emission in the 16-μm band using the *Spitzer Space Telescope*. Photometry enabled a clear detection of the eclipse with a depth of 0.551 ± 0.030 per cent, or $F_\mathrm{p}/F_* = 0.0055 \pm 0.0003$, indicating the star to be only 181 times brighter than the planet at 16 μm near to eclipse.

Tinetti et al. (2007a) modelled transmission spectra, which are dominated by H_2O and CO opacities, and presented simulations to show that these features should be deep enough to produce signatures which are detectable in the thermal infrared by present and future space based missions. Tinetti et al. (2007b) have subsequently used planetary transit depth observations made with the *Spitzer Space Telescope* Infrared Array Camera (IRAC) at 3.6 μm, 5.8 μm (see Tinetti et al. 2007b) and 8 μm (Knutson et al. 2007) in conjunction with transmission spectra modelled using H_2O opacity lists (Barber et al. 2006) to infer the presence of water in the atmosphere of HD 189733b. Grillmair et al. (2007), however, have reported measurement of the 7.5–14.7 μm spectrum of HD 189733b using the *Spitzer Space Telescope* Infrared Spectrograph (IRS) which does not show the expected decrease (Burrows, Sudarsky & Hubeny 2006) in flux at the short-wavelength end of this range due to increasing H_2O opacity. It has been suggested (Fortney & Marley 2007) that the discrepancy between the IRAC 8-μm flux and IRS flux may result from unreliable reduction of the IRS spectra and that the IRAC photometry is thus in good agreement with one-dimensional atmospheric models of HD 189733b in the 8–16 μm range spanned by IRAC flux measurements.

Knutson et al. (2007) observed 0.12 per cent flux variation between transit and secondary eclipse, with a maximum 16° before secondary eclipse. Their 8-μm *Spitzer* observations were used to derive a simple surface map showing a hot spot offset by 30° east of the substellar point.

In this paper, we aim to detect the absorption signature of HD 189733b at ∼2.2 μm. The method outlined in Section 3 has the potential to determine the planet/star contrast ratio, F_p/F_*, if an absorption signature is detected (Barnes et al. 2007). The detection of such opacities forms an important test for the presence of atmospheric molecular species.

2 OBSERVATIONS AND DATA REDUCTION

Observations were made with NIRSPEC (McLean et al. 1998) at the Keck II Telescope on UT 2006 July 22. A high-cadence time series of HD 189733 spectra was recorded using a 1024 × 1024 InSb Aladdin-3 array. The rapidly rotating bright A0V star, HD 192538, was observed at the start of the night to enable identification of telluric features in the spectra. With the NIRSPEC-7 blocking filter, a wavelength span of 2.0311–2.3809 μm was achieved at a resolution of $R \sim 15\,000$. The observations are summarized in Table 1.

2.1 Data extraction

Each raw frame was corrected by subtracting a scaled dark current frame. Pixel to pixel variations were removed using flat-field exposures taken with an internal tungsten reference lamp. In order to create a reliable balance frame to remove the pixel sensitivity variations, we divided a Gaussian blurred (using a full width at half-maximum of 7 pixel) version of the master flat-field image by the original master flat-field image. Two flat-fields each comprising of

Table 1. NIRSPEC/Keck II observations of HD 18733 and HD 192538 for UT 2006 July 22. Cloud cover was highly variable throughout the night. Groups of 15 spectra from the first HD 189733 block were co-added post-observations to give the same effective exposure time (60 s) as in the second block, resulting in an effective total of 238 frames. As a result of variable cloud cover, we were unable to extract 13 of the HD 189733 spectra, leaving 225 usable frames.

Object	UT start of first frame	UT start of last frame	Time per exposure (s)	Number of co-adds per frame	Number of observations	Comments
			UT 2006 July 22			
HD 192538	05:48:46	05:59:18	60	1	8	A0V template
HD 189733	06:10:58	06:43:52	4	1	125	Software crash at the end of sequence
HD 189733	07:04:27	14:08:0922	4	15	230	

100 median-combined frames taken at both the start and end of the night were used since a software crash at the end of the first sequence of frames listed in Table 1 resulted in an instrument reset. After reboot, a small shift of 2 pixels in wavelength position of the grating occurred. An examination of the balance frames shows that while blemishes and hot pixels remain unchanged, a striped or interference pattern present in the balance frame taken at the start of the night has shifted in the balance frame taken at the end of the night. The interference pattern varies from order to order and repeats with a length-scale of between 10 and 20 pixel. If this pattern is purely dependent on the light path, it should largely be removed as a result of flat-fielding. By dividing one balance frame by the other, and measuring the residual in each order, we estimate the flat-field stability limited by shifts in the interference pattern after instrument set-up changes (2 pixel shift) through the night to be 1.0 per cent. The flat-field at the start of observations was used for the first block of observations which only comprised eight sets of co-added frames (Table 1, see caption), while the flat-field taken at the end of observations was used in conjunction with the remainder of observations after the instrument was reset.

The worst cosmic ray events were removed at the pre-extraction stage using the Starlink FIGARO routine BCLEAN (Shortridge 1993). The recorded frames comprised 4-s exposures at the start of the night before the software crash (see Table 1) and $15 \times 4 = 60$ s exposures thereafter. We therefore co-added groups of 15 exposures from the first set of frames to ensure that all spectra were exposed for the same 60 s.

A number of sky lines were present in the four shortest wavelength orders while the two reddest orders contained only one very weak line. In order to maximize the stability of observations made with the instrument, we decided against using a nodding ABBA sequence. We were thus unable to use subsequent A−B and B−A differences to reject sky lines during the extraction. We followed a similar method to that detailed in Barnes et al. (2007), finding that the Starlink échelle data reduction package, ECHOMOP (Mills 1994), rejects all but one strong sky line, at ∼21 501.5 Å through iterative fitting of a third-degree polynomial. Bad pixels on the detector close to the location of this strong sky line meant that a small region encompassing the line was excluded from further analysis. The spectra were extracted using ECHOMOP's implementation of the optimal extraction algorithm developed by Horne (1986). ECHOMOP propagates error information based on photon statistics and readout noise throughout the extraction process.

2.2 Wavelength calibration

Calibration frames using a combination of Ar, Ne, Xe and Kr lamps were taken during the observations although the line identifications are poor in some orders. We therefore adopted the approach used in Barnes et al. (2007) where telluric features in the observed spectrum of the standard star were used. A spectrum generated from a high-resolution transmission molecular absorption database line list (Rothman et al. 2005) enabled identification of the corresponding features with known/measurable wavelengths. Between 10 and 19 lines were used in each order and a cubic polynomial was used to give fits with a rms scatter equal to 1.44×10^{-6} μm (0.0144 Å). The mean wavelength increment of the six calibrated orders (NIRSPEC orders 32–37) is 3.23×10^{-5} μm (0.323 Å). At the 2.185-μm centroidal wavelength position of our deconvolved lines (see Section 3.3), the rms scatter in the fit corresponds to 0.045 pixel elements or 0.00 099 resolution elements. The wavelength ranges for each of the six orders are: 2.031–2.061 μm (order 37), 2.087–2.118 μm (order 36), 2.146–2.178 μm (order 35), 2.209–2.242 μm (order 34), 2.275–2.309 μm (order 33) and 2.346–2.381 μm (order 32).

3 SEARCHING FOR A PLANETARY SIGNATURE

3.1 Removal of stellar and telluric spectra

Before searching for a planetary signal, it is important to remove the stellar and telluric lines from our spectra. This is achieved by subtracting a shifted and scaled template spectrum that has been created by co-adding all the frames from our night of observations. This procedure is valid because the planetary signal is not stationary during the observations. The phases of the observations made here mean that any planetary absorption signature will be Doppler shifted from $+60$ to -80 km s^{-1} during the planet's orbit about HD 189733. The template spectrum was fitted to each HD 189733 spectrum in turn by taking derivatives of the spectra and using splines to calculate the scale factor at points across the spectra. This process can account for those lines that behave independently over the night and is described in Collier Cameron et al. (2002, appendix A). For example, all telluric lines do not necessarily vary in strength by the same factor at any given time while the strength of all telluric lines may vary relative to the stellar lines. Fig. 1 (tick marks at bottom of each panel) shows the positions of stellar lines (for further details see Section 3.3) from the Vienna Atomic Line data base (Kupka et al. 1999). A comparison with the observed template spectrum above the tick marks shows that the spectra are dominated by the telluric lines.

While this template subtraction procedure is effective at removing the stellar and telluric lines and preserving a possible planetary signal, some residuals remain in the spectra. These residuals often appear in blocks of spectra and become evident when each echelle order is displayed in a grey-scale image. The large variability in signal-to-noise ratio (S/N) of the current spectra (Section 3.3), due to highly variable cloud cover, prompted us to investigate removal of the blocks of spectra containing the fewest counts. In Section 4, we report our findings for the case where 42 per cent of the spectra were rejected prior to further analysis.

Remaining systematics were removed using principal components analysis as described by Collier Cameron et al. (2002, appendix B), and discussed at length in Barnes et al. (2007). A balance must be struck between removal of systematics and removal of photons which would reduce our detection threshold. Only residuals at a fixed wavelength position are removed if the first few principal components are subtracted from the data, ensuring a moving planetary signal is not significantly attenuated. We subdivided each of the six orders into three sections and subtracted the strongest components (between 2 and 5) for each section.

3.2 Atmospheric model

We attempt to make optimal use of the information content of our spectra by considering all the planetary absorption lines contained within the ∼1645 Å wavelength span of our data. We therefore require a model that describes the planetary atmosphere as accurately as possible. Barnes et al. (2007) discuss the nature of the irradiated model atmosphere that includes day-night time temperature gradients on the planet. For a full description of the model opacities and set-up see Ferguson et al. (2005), Barman, Hauschildt & Allard (2001) and Barman, Hauschildt & Allard (2005, hereafter BHA05). For HD 189733b, we model an atmosphere with solar metallicity

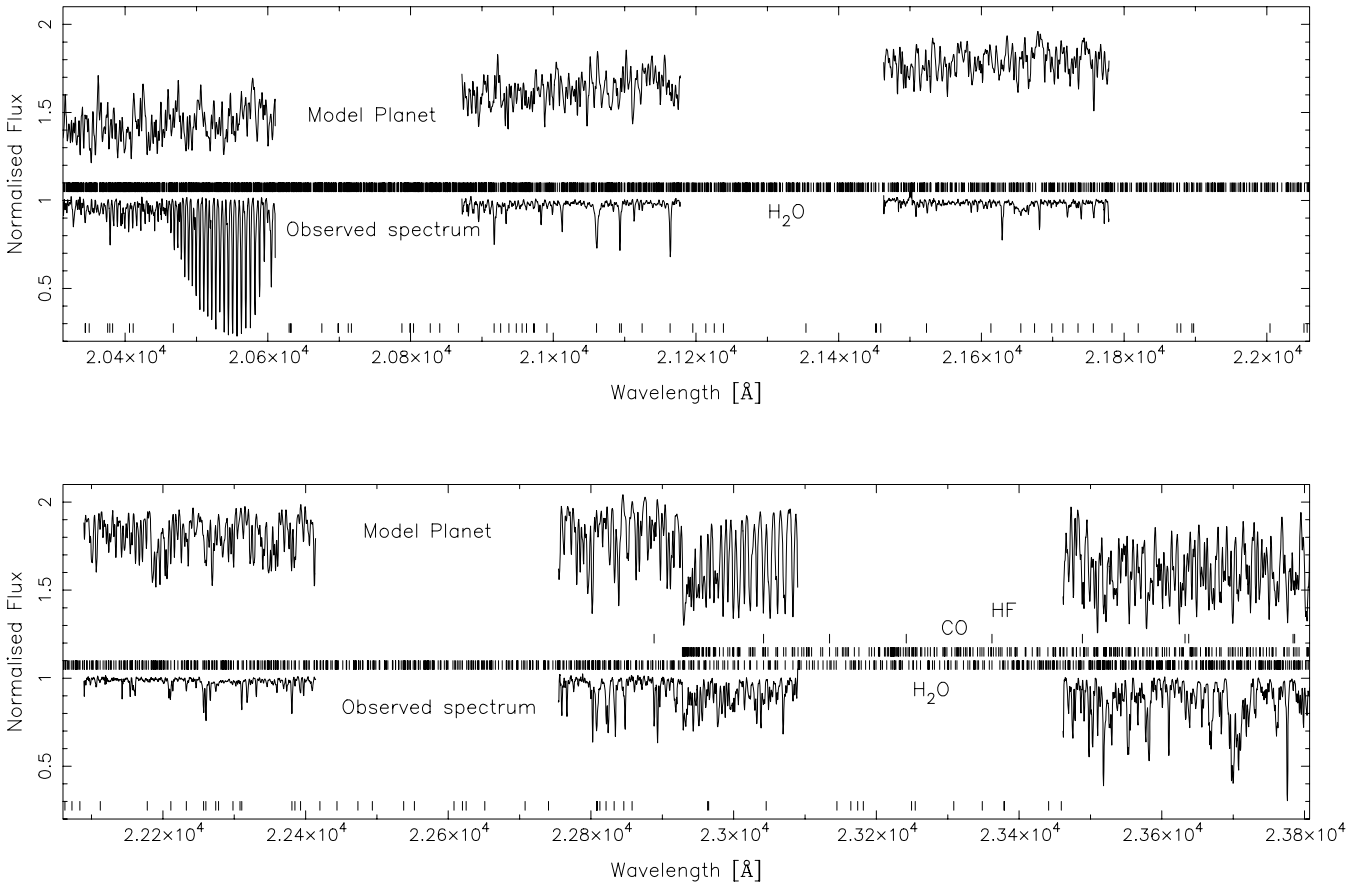

Figure 1. Model planet (top in each panel) spectrum and observed spectrum (bottom in each panel) for NIRSPEC orders 37, 36, 35, 34, 33 and 32 (top to bottom, left- to right-hand side). Each spectrum spans 2.03–2.38 μm at a resolution of $R \sim 15\,000$. The model planetary spectrum has been degraded to the same instrumental resolution and broadened with a rotation profile of width 2.53 km s^{-1} in accordance with a tidally locked planet with the empirically determined parameters of HD 189733b. The gaps between spectra show the regions not covered by the instrumental set-up (see Section 2.2). The planetary spectrum is shown in the absence of any stellar host and in reality would be weaker by a factor equal to the planet/star contrast ratio, F_p/F_*. The tick marks at the bottom of each panel represent the theoretical positions of Fe and Si stellar lines as given by the Vienna Atomic Line Database for a $T = 5000$ K spectrum. The tick marks in the middle of each panel mark the positions of the strongest expected planetary opacities from our model (labelled accordingly from bottom to top as H_2O, CO and HF) demonstrating H_2O to be the dominant species. The HF and CO opacities begin at 2.2895 and 2.2935 μm, respectively.

for a temperature, $T = 1250$ K and surface gravity, $\log g = 1.33$ m s^{-1}.

In Barnes et al. (2007), the modelled planet, HD 75289b, was not as close to the G0V parent star ($a = 0.0482$ au) as HD 189733b is to its K2V host ($a = 0.0312$ au). The opacities that remain after rainout of condensed species has occurred (such as TiO and VO) appear stronger for HD 189733b when compared with HD 75289b (Barnes et al. 2007) and are due to two main species, namely H_2O and CO, in the wavelength region of our data. Fig. 1 shows the wavelength range of our data where the tick marks represent strongest H_2O, CO and HF opacities. The detection method used to search for a planetary signature (Sections 3.3 and 3.4) is model-dependent and may be affected by a number of factors. Missing or incorrect line opacities in the model are potential problems; however, the line opacities used in the model are known to be fairly reliable for similar temperatures and pressures found in brown dwarfs (Freedman, Marley & Lodders 2007). In Barnes et al. (2007), we investigated the effects of a mismatch in line opacity strengths and line positions for a similar instrumental set-up to that used for the observations in this paper. We found that the simulations still enabled us to detect a planetary signal with 99.9 per cent confidence (a 1.58 times drop in planet/star ratio) for the case where the model line list line strengths used in deconvolution were modified by 50 per cent or for the case where the 15 per cent of the line opacity wavelengths were randomized. The H_2O line lists used in our model are taken from Barber et al. (2006) and represent the most complete and accurate water line lists to date.

3.3 Deconvolution

A line list (comprising opacity wavelength positions and line depths) based on the model atmosphere described in Section 3.2 is used as a deconvolution template for planetary absorption features which are hidden within each HD 189733b spectrum. The least-squares deconvolution procedure yields a single mean absorption line for each HD 189733b spectrum which when scaled with the line list gives the best fit to the observed spectrum. In this way, the effective S/N of the mean deconvolved absorption line is much higher than that of individual lines, potentially enabling a weak signal to be extracted from the data. The method of least-squares deconvolution was first described by Donati et al. (1997). Our implementation of the algorithm (Barnes et al. 1998) propagates errors from the input spectra and has been used in reflected light searches in the optical by Collier Cameron et al. (1999, 2002) and Leigh et al. (2003a,b). A

detailed description of the use of this algorithm with near-IR spectra is described in Barnes et al. (2007).

Of the 225 usable spectra, the mean S/N, measured from residual spectra after removal of the template, was 136 ± 85. The minimum and maximum S/N were 27 and 382, respectively, with only 10 per cent of the spectra possessing S/N > 250. We assess the consequences of this highly variable S/N in Section 4. Since the spectra are dominated by very strong telluric lines in the 2.0445–2.0610 μm region of order 37 and the 2.3650–2.3807 μm region of order 32 (Fig. 1), we did not use these regions in the deconvolution procedure. The gain in S/N of 20 for the mean deconvolved spectrum yielded S/N of 2751 ± 1772. The full range of S/N in the deconvolved spectral profiles is, however, 540–7640, again, reflecting the highly variable cloud conditions throughout the night of observations.

3.4 Matched filter

We model the time-dependent changes in Doppler shift and brightness using a matched filter analysis described in detail in appendix D of Collier Cameron et al. (2002). Modifications of this implementation are described in Barnes et al. (2007), but we reiterate the basics of the procedure here for clarity.

We model a travelling Gaussian which traces out the motion of HD 189733b in an assumed circular orbit about its host star. The radial velocity motion of the planet as a function of phase thus traces out a sinusoid. We assume the planet to be tidally locked and use a model describing the variation in brightness of an irradiated planet that possesses a hot inner face with little redistribution of heat. We assume, as found in Barnes et al. (2007), that this variation closely resembles a Venus-like phase function (Hilton 1992). Discussion of the true nature of the phase function is discussed in more detail in Section 5 in light of recent observations, although we note here that a Venus-like phase function agrees with these findings to within 5 per cent over the range of phases of our observations. We asses the relative probabilities of the χ^2 fits to the data by varying the peak contrast ratio, $\epsilon_0(\lambda)$, and the velocity amplitude of the orbital motion, K_p. The peak contrast ratio occurs at secondary eclipse (i.e. phase $\phi = 0.5$) in the case of a Venus-like phase function. In the phase range ($0.44 < \phi < 0.59$) of our data, we are sampling the region of the sinusoid where, to first order, the radial velocity motion approximates a straight line. The gradient of this line, which is fitted by a sinusoid in our model, thus enables an estimate of the velocity amplitude, K_p, to be made. The improvement in χ^2 is estimated for combinations of these parameters and is normalized relative to the best-fitting model. To calibrate any candidate detection, we construct a simulated planet signal of known $\epsilon_0(\lambda)$, with $\lambda = 2.185$ μm that is added to the extracted spectra prior to analysis. By ensuring the fake planet is recovered at the correct contrast ratio (hereafter, simply ϵ_0 or $\log_{10}\epsilon_0$) by our procedures, we can be confident of a detection in the presence of a genuine planet signal.

The significance of the result is assessed using bootstrap statistical procedures based on the random re-ordering of the data in a way that scrambles phases while preserving the effects of any correlated systematic errors (Collier Cameron et al. 2002). The order of the observations is randomized in a set of 3000 trials which will scramble any true planetary signal while enabling the data to retain the ability to produce spurious detections through the chance alignment of systematic errors. The least-squares estimate of $\log_{10}\epsilon_0$ and associated χ^2 as a function of K_p enable us to plot 68.4, 95.4, 99.0 and 99.9 per cent bootstrap limits on the strength of the planetary signal.

4 RESULTS

In Fig. 2 (left-hand side), we plot the deconvolved spectral time series. The dashed line is plotted as a guide for the reader and represents the velocity path of a planet with the same parameters as determined empirically for HD 189733b. We can obtain an estimate of the velocity amplitude of the planet by taking $a = 0.0312 \pm 0.0004$ au $P = 2.218\,5733 \pm 0.000\,0019$ d and $i = 85.76 \pm 0.^\circ29$, from which we find $v_\mathrm{p} = 152.58 \pm 1.96$ km s^{-1}. We discuss additional factors that could augment this uncertainty in Section 5. Fig. 2 (right-hand side) presents the result of our matched Gaussian filter analysis. Again, the dashed line represents the velocity at which HD 189733b should appear. The darkest regions in the map represent the greatest improvement in χ^2 when fitting the model described in Section 3.3. In the optical studies carried out by Collier Cameron et al. (1999, 2002) and Leigh et al. (2003a,b), the reflected light signal was simply an attenuated copy of the stellar spectrum. The central portion of the deconvolved time series was excluded during the matched filter modelling to ensure that no spurious signal due to remaining residuals of an inadequately subtracted stellar profile were included. Here, however, the planetary spectrum is not expected to be a copy of the stellar spectrum and any line opacities should be randomly distributed with respect to stellar opacities in the spectrum. However, since HD 189733b is a transiting planet, when applying our matched filter analysis, we exclude the portion of spectrum when the planet is not visible. Winn et al. (2007) estimate a transit time of 1.827 ± 0.029 h indicating that the planet is not visible for phases $0.483 < \phi < 0.517$.

The feature at $K_\mathrm{p} \sim 52$ km s^{-1} is the result of remaining systematics in the deconvolved time series. To enhance the grey-scale in the region of the χ^2 map where we know HD 189733b should appear, as outlined above, we excluded $K_\mathrm{p} < 100$ km s^{-1} when computing the grey-scale, resulting in a dark block in the map around the $K_\mathrm{p} \sim 52$ km s^{-1} feature. We do not detect the planet with 1 and 2σ confidence at levels of $\log_{10}\epsilon_0 = \log_{10}(F_\mathrm{p}/F_*) = -3.26$ and -2.72, respectively. The equivalent star/planet contrasts are $F_*/F_\mathrm{p} = 1820$ and 525, respectively.

Fig. 2 (top left panel) shows clear systematic features, which are not subtracted, even after removing the first two to five principal components as outlined in Section 3.1. This is especially notable for spectra taken in the phase range $0.52 < \phi < 0.54$. We attribute these residuals to variation in telluric strengths throughout the night and as a result of the highly variable cloud cover. Since the observations were made at a spectral resolution of $R \sim 15\,000$, it is not possible to effectively scale the template spectrum in all regions, especially where those telluric features that may vary in strength independently are blended.

To investigate the effect of the highly variable S/N, we rejected frames with the lowest S/N. A threshold level that removed the main blocks of lower S/N spectra (S/N < 97) was chosen, leaving 131 spectra. The deconvolved profiles (Fig. 2, bottom left panel) possess S/N = 3800 ± 1480. The matched filter analysis performed on these spectra alone enables us to place 1σ and 2σ confidence at levels of $\log_{10}\epsilon_0 = -3.40$ and -2.88 on a non-detection of HD 189733b (Fig. 2, bottom right). The equivalent star/planet contrasts are $F_*/F_\mathrm{p} = 2512$ and 759, respectively. We are nevertheless able to improve the sensitivity of our result, although at the 1σ level, the results are indistinguishable. Despite using fewer spectra, we believe that an increased sensitivity is due to the reduced range of S/N values of our spectra. The systematic effects introduced by unresolved telluric features, which cannot easily be corrected for (Bailey, Simpson &

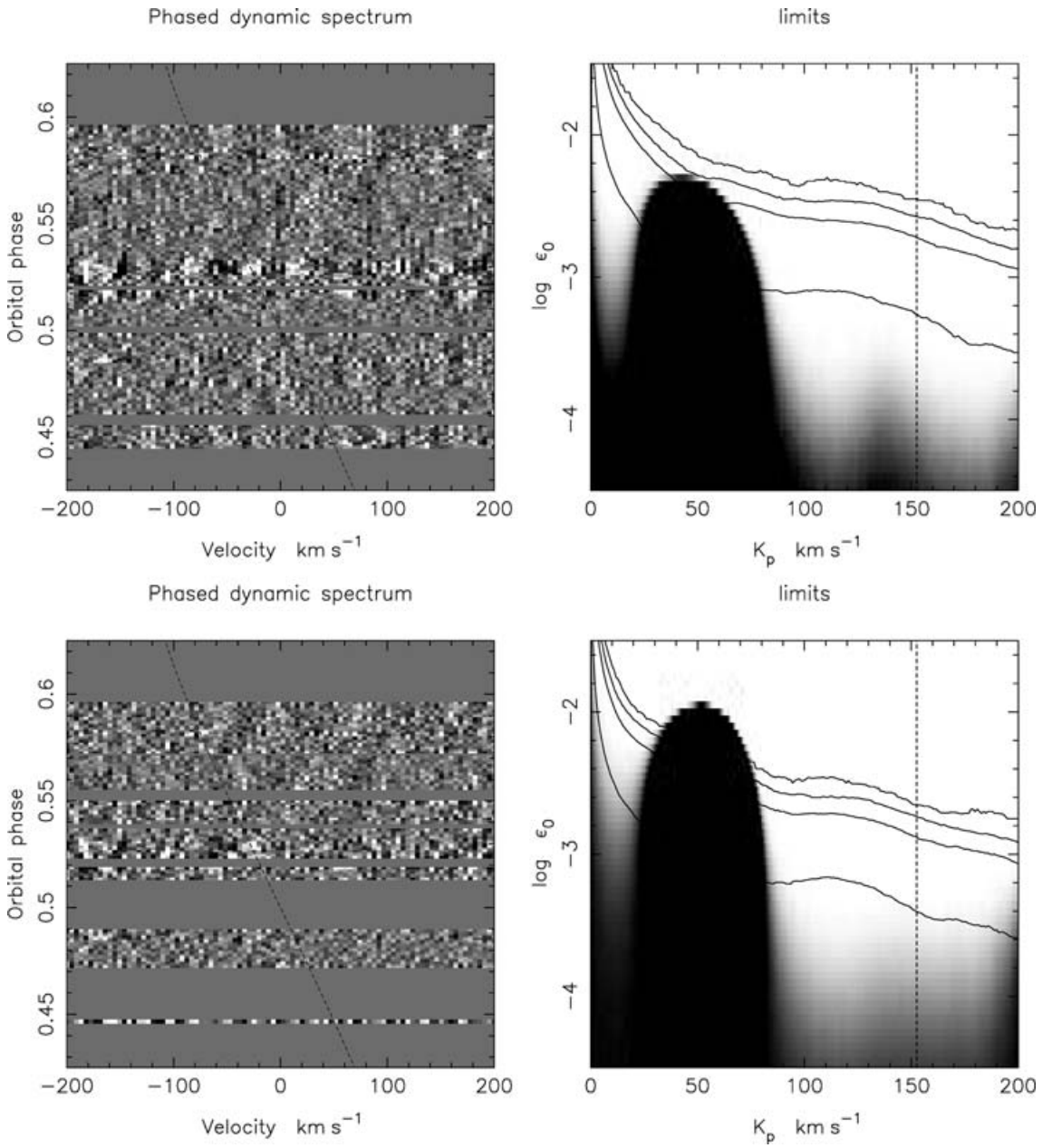

Figure 2. Left-hand side: phased time series of the deconvolved residual spectra of HD 189733. The dashed sinusoidal curve represents the *expected* motion of a planetary signal based on the empirically determined velocity amplitude, $K_{\rm p} = 152.8 \pm 2.0$ km s^{-1}. Since the S/N is variable, for plotting purposes, all deconvolved profiles have been normalized to the same noise level to optimize the visible information content of the plot. Right-hand side: relative probability χ^2 map of planet-star flux ratio $\log_{10}\,\epsilon_0$ versus $K_{\rm p}$. The first two to five principal components have been subtracted from the time series spectra. The grey-scale in the probability maps represents the probability relative to the best-fitting model in the range $100 < K_{\rm p} \leqslant 200$ km s^{-1} in the range white for 0 to black for 1. A candidate feature with $K_{\rm p} = 52$ km s^{-1} resulting from systematics (see the main text) has resulted in the large dark region in the left-hand side of the plot. Plotted are the 68.3, 95.4, 99 and 99.9 per cent (bottom to top) confidence levels for a planetary signal detection. The dashed vertical line represents the velocity amplitude, $K_{\rm p} = 152.8$ km s^{-1}. No planetary signal is detected at this velocity. Top panel: analysis using all 225 spectra. Bottom panel: analysis after removal of blocks of the lowest S/N spectra. Using the remaining 131 deconvolved spectra results in the same confidence levels appearing at lower contrast ratios.

Crisp 2007), are thus a critical factor in determining the sensitivity of our technique.

5 DISCUSSION

The near-IR planet/star contrast ratio, $F_{\rm p}/F_*$, offers a much more favourable regime over optical wavelengths in which to carry out a search for a planetary signal. The technique, in addition to offering a chance to determine the contrast ratio, relies upon our ability to detect absorption in the planetary atmosphere. The contrast limit placed by this study is intriguing because we do not detect the planet at a level of $F_{\rm p}/F_*$ that is 1.7 times less than the model prediction; and despite the observation that our model is in agreement with mid-infrared *Spitzer* observations (Deming et al. 2006; Grillmair et al. 2007; Knutson et al. 2007). Fig. 3 is a plot of the theoretical $F_{\rm p}/F_*$ from our model indicating both the mid-infrared *Spitzer*

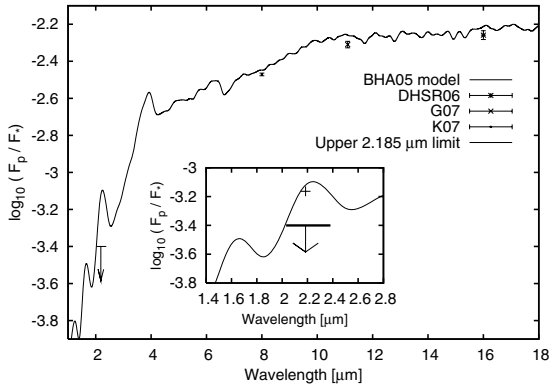

Figure 3. Model planet/star flux ratio for the HD 189733 system. A *Spitzer* eclipse depth measurement using the IRAC is plotted for 8 μm (Knutson et al. 2007, hereafter K07). Similar measurements using the *Spitzer* Infrared Spectrograph (IRS) are plotted for 11.1 μm (Grillmair et al. 2007, hereafter G07) and 16 μm (Deming et al. 2006, hereafter DHSP06). A horizontal bar with vertical down-pointing arrow indicates our 2.185 μm 1σ upper limit. The width of the horizontal bar represents the wavelength range of our data. The single point plotted in the inset at $\log_{10}\epsilon_0 = -3.16$ represents the model mean flux over this range. The upper limit is at a level of $\log_{10}\epsilon_0 = 0.24$ lower than the model [i.e. ϵ_0(model)/ϵ_0(observed) = 1.7].

measurements and the upper limit determined above. For comparison with the Barnes et al. (2007) simulations, a non-detection at the reported level may arise if 55 per cent of line strengths are mismatched or 16 per cent of the lines possess incorrect wavelengths (see Section 3.2).

Apart from line position and strength mismatches between model and observed spectra, another possibility that would result in a non-optimal search for the planetary signature is use of an incorrect phase function. Barnes et al. (2007) found a Venus-like phase function for the HD 75289 models over the phases of observation considered. The overall variation in flux found by Knutson et al. (2007) indicates that a Venus-like phase function is less appropriate for HD 189733b, indicating that heat is more effectively transported in its atmosphere. The lower contrast between night and day yields a temperature range of 973–1212 K. Over the small range of our observations, however, we find that the variation in flux from the maximum as observed by Knutson et al. (2007) is consistent with a Venus-like phase function to within 5 per cent.

Harrington et al. (2006) measured the phase-dependent flux of υ and b, finding variation that was well fitted by the models of BHA05, implying poor transfer of thermal energy. On the other hand, the more recent observations by Knutson et al. (2007) found that a maximum in flux for the HD 189733 system occurred at a phase angle of 16° before mid-eclipse of the planet. They derived a surface map of HD 189733b and found the hottest part of the atmosphere is offset 30° east of the substellar point. We adjusted our Venus-like phase function by 16° to ensure a maximum occurred at the same phase (i.e. $\phi = 0.456$) rather than at phase $\phi = 0.5$. This did not result in the appearance of a candidate planetary feature in our χ^2 map, however. The resulting *increase* of the 1σ confidence level from $\log\epsilon_0 = -3.4$ to -3.25 is equivalent to a reduction in sensitivity by a factor of 1.4. This is probably the result of shifting the time at which the planetary flux maximum occurs to the phase where observations began. As can be seen in Fig. 2 (bottom left panel), only one observation is made before maximum when the shifted phase function is used.

Nevertheless, the possibility that the observed phase function peak may be a function of wavelength is supported by simulations. Cooper & Showman (2005) and Cooper & Showman (2006) carried out three-dimensional atmospheric circulation simulations for HD 209458b and found that the circulation pattern is a function of atmospheric pressure or depth. In the lower pressure regime of the outer atmosphere, the radiative time-scale is much shorter than advective time-scales such that absorbed stellar heat is quickly re-radiated. Lower in the atmosphere, at higher pressures, advective time-scales become important and carry absorbed energy in an easterly direction. Based on these models, Fortney et al. (2006) has shown that the location of the phase function peak is indeed expected to be a function of wavelength in the case of HD 209458b. The time at which the phase function peak occurs before secondary eclipse is inversely proportional to wavelength, in agreement with the findings of Harrington et al. (2006) and Knutson et al. (2007). This implies that shorter wavelengths probe deeper layers of the planetary atmosphere. Wind speeds of the order of 6.6 to 4.3 km s^{-1} at 10 mbar to 1 bar respectively in an easterly direction are high, and while not sufficient to significantly shift the apparent velocity amplitude of the planet (e.g. see Fig. 2), they introduce an additional factor into the error budget of the estimated 1.96 km s^{-1} uncertainty (Section 4). An easterly wind flow would act to reduce the apparent velocity amplitude, but since most of the planetary signal is expected to come from the hotspot which would be travelling transversely to the observer at the observed phases, any induced perturbation is likely to be a second-order effect.

Although Fortney et al. (2006) only model HD 209458b it seems reasonable to expect that our ∼2.2-μm observations also probe deeper layers of the atmosphere of HD 189733b. If the temperature–pressure gradient is lower or even flat in this regime (i.e. 100 mbar–1 bar), as indicated for HD 209458b in BHA05, it may be that absorption lines are suppressed and the dayside spectrum approaches that of a blackbody. Also, the reasonable agreement between the hotter no-redistribution model and the *Spitzer* observations (that emerge from layers above the *K*-band photosphere), may be an indication of a deeper temperature structure cooled by energy redistribution to the night side, similar to what has been predicted for HD 209458b by Cooper & Showman (2005). Constraints on the depth-dependent redistribution in the atmosphere of HD 189733b will be explored in more detail by Barman et al. (in preparation).

6 CONCLUSION

The methods presented here provide a powerful technique with which to detect a planetary absorption signature and the 1σ $\log_{10}\epsilon_0 = -3.40$ limit is extremely interesting. We have outlined a number of possibilities for the lack of detection of a planetary signal. Our data suggest that ideal observing conditions would enable us to obtain spectra with S/N as high as ∼380. With the same NIRSPEC instrumental set-up at Keck II, a total of 230 frames with S/N = 300 taken over the same orbital phase range would enable us to push our 1σ and 2σ limits down to levels of $\log_{10}\epsilon_0 = -3.90$ and 3.40, respectively. Also, the high variability of the stellar flux relative to the telluric lines (due to highly variable cloud cover) seen in our present data would be reduced in more ideal conditions. This would lead to fewer systematics after template spectrum removal enabling us to further lower our confidence level estimates for ϵ_0. Additionally, observations at higher spectral resolution than currently afforded by the present data would be desirable, as demonstrated in Barnes et al. (2007), and would lead to better telluric subtraction.

An independent, near-IR, photometric detection would enable us to place stronger limits on the reliability of the line list parameters or the nature of the atmosphere itself. For instance, when combined

with spectral observations, as described above, it would be possible to rule out or place limits on the presence of absorption features in the corresponding wavelength region.

ACKNOWLEDGMENTS

JRB was supported by a PPARC funded research grant during the course of this work. TB acknowledges support from NASA's Origins of Solar system program and the NASA Advanced Supercomputing facility, and LP from NSF grant 04-44017. The data presented herein were obtained at the W. M. Keck Observatory, which is operated as a scientific partnership among the California Institute of Technology, the University of California and the National Aeronautics and Space Administration. The Observatory was made possible by the generous financial support of the W. M. Keck Foundation. The authors wish to recognize and acknowledge the very significant cultural role and reverence that the summit of Mauna Kea has always had within the indigenous Hawaiian community. We are most fortunate to have the opportunity to conduct observations from this mountain.

REFERENCES

Bailey J., Simpson A., Crisp D., 2007, PASP, 119, 228
Bakos G. Á. et al., 2006a, ApJ, 650, 1160
Bakos G. Á., Pál A., Latham D. W., Noyes R. W., Stefanik R. P., 2006b, ApJ, 641, L57
Barber R. J., Tennyson J., Harris G. J., Tolchenov R. N., 2006, MNRAS, 368, 1087
Barman T. S., Hauschildt P. H., Allard F., 2001, ApJ, 556, 885
Barman T. S., Hauschildt P. H., Allard F., 2005, ApJ, 632, 1132 (BHA05)
Barnes J. R., Collier Cameron A., Unruh Y. C., Donati J. F., Hussain G. A. J., 1998, MNRAS, 299, 904
Barnes J. R., Leigh C. J., Jones H. R. A., Barman T. S., Pinfield D. J., Collier Cameron A., Jenkins J. S., 2007, MNRAS, 379, 1097
Bouchy F. et al., 2005, A&A, 444, L15
Burrows A., Sudarsky D., Hubeny I., 2006, ApJ, 650, 1140
Charbonneau D., Noyes R. W., Korzennik S. G., Nisenson P., Jha S., Vogt S. S., Kibrick R. I., 1999, ApJ, 522, L145
Collier Cameron A., Horne K., Penny A., James D., 1999, Nat, 402, 751
Collier Cameron A., Horne K., Penny A., Leigh C., 2002, MNRAS, 330, 187
Cooper C. S., Showman A. P., 2005, ApJ, 629, L45
Cooper C. S., Showman A. P., 2006, ApJ, 649, 1048
Deming D., Seager S., Richardson L. J., Harrington J., 2005, Nat, 434, 740
Deming D., Harrington J., Seager S., Richardson L. J., 2006, ApJ, 644, 560 (DHSP06)
Donati J.-F., Semel M., Carter B., Rees D. E., Collier Cameron A., 1997, MNRAS, 291, 658
Ferguson J. W., Alexander D. R., Allard F., Barman T., Bodnarik J. G., Hauschildt P. H., Heffner-Wong A., Tamanai A., 2005, ApJ, 623, 585
Fortney J. J., Marley M. S., 2007, ApJ, 666, L45
Fortney J. J., Cooper C. S., Showman A. P., Marley M. S., Freedman R. S., 2006, ApJ, 652, 746
Freedman R. S., Marley M. S., Lodders K., 2007, ApJS, in press (arXiV: 0706.2374)
Grillmair C. J., Charbonneau D., Burrows A., Armus L., Stauffer J., Meadows V., Van Cleve J., Levine D., 2007, ApJ, 658, L115 (G07)
Harrington J., Hansen B. M., Luszcz S. H., Seager S., Deming D., Menou K., Cho J. Y.-K., Richardson L. J., 2006, Sci, 314, 623
Hilton J., 1992, Expanatory Supplement to the Aastronomical Almanac. University Science Books, Mill Valley, CA
Horne K. D., 1986, PASP, 98, 609
Kaüfl H.-U. et al., 2004, in Moorwood A. F. M., Iye M., eds, Proc. SPIE Vol. 5492, Ground-based Instrumentation for Astronomy. SPIE, Bellingham, p. 1218
Knutson H. A. et al., 2007, Nat, 447, 183 (K07)
Kobayashi N. et al., 2000, in Iye M., Moorwood A. F., eds, Proc. SPIE Vol. 4008, Optical and IR Telescope Instrumentation and Detectors. SPIE, Bellingham, p. 1056
Kupka F., Piskunov N., Ryabchikova T. A., Stempels H. C., Weiss W. W., 1999, A&AS, 138, 119
Leigh C., Cameron A. C., Horne K., Penny A., James D., 2003a, MNRAS, 344, 1271
Leigh C., Collier Cameron A., Udry S., Donati J.-F., Horne K., James D., Penny A., 2003b, MNRAS, 346, L16
McLean I. S. et al., 1998, in Fowler A. M., ed., Proc. SPIE Vol. 3354, Infrared Astronomical Instrumentation. SPIE, Bellingham, p. 566
Mills D., 1994, Technical Report 152, Starlink User Note. Rutherford Appleton Laboratory
Rothman L. S. et al., 2005, J. Quant. Spectrosc. Radiat. Transfer, 96, 139
Rowe J. F. et al., 2006, ApJ, 646, 1241
Shortridge K., 1993, in Hanisch R. J., Brissenden R. J. V., Barnes J., eds, ASP Conf. Ser. Vol. 52, Astronomical Data Analysis Software and Systems II. Astron. Soc. Pac, San Francisco, p. 219
Tinetti G., Liang M.-C., Vidal-Madjar A., Ehrenreich D., Lecavelier des Etangs A., Yung Y. L., 2007a, ApJ, 654, L99
Tinetti G. et al., 2007b, Nat, 448, 169
Winn J. N. et al., 2006, ApJ, 653, L69
Winn J. N. et al., 2007, AJ, 133, 1828

This paper has been typeset from a TEX/LATEX file prepared by the author.